Construction and Building Materials 355 (2022) 129228

Contents lists available at ScienceDirect

Construction and Building Materials

journal homepage: www.elsevier.com/locate/conbuildmat

Characterizing the bond properties of automatically placed helical reinforcement in 3D printed concrete

Lauri Hass [a,b,*], F.P. Bos [a,c], T.A.M. Salet [a]

[a] Eindhoven University of Technology, 5612 AZ Eindhoven, The Netherlands
[b] Tallinn University of Technology, Department of Civil Engineering and Architecture, Tallinn, Estonia
[c] Technical University of Munich, School of Engineering and Design, Chair of Concrete and Masonry Structures, Munich, Germany

ARTICLE INFO

Keywords:
Helical reinforcement
Bond characterization
Automated placement system
3DCP

ABSTRACT

The incompatibility of 3D concrete printing (3DCP) with conventional reinforcement methods is well known. Recently, solutions have suggested the insertion of helical reinforcement rods through a screwing motion into the freshly printed material. The current study focuses on the bond properties of such reinforcement and its relation to placement time relative to the 3D printed concrete age, of which until now hardly any data exists. Confined pull-out tests and micro-computed tomography (μCT) scans were performed to characterize the time-dependent bond properties for automatically placed screw-type reinforcement in 3D printed concrete in the range of 0–200 min after material deposition. An experimental program was carried out using a gantry type 3D concrete printer and a robotic hand with the Automated Screwing Device to automate the reinforcement placement process. In total 200 specimens were produced and tested in pull-out. μCT scans were done on the specimens to quantify air content in the vicinity of the reinforcement, for every other time stamp. Two different screw geometries were used. A high mechanical interlock was achieved resulting in a high bond strength in confined pull-out tests. It was concluded from the confined pull-out tests that the pull-out performance is not influenced significantly by the time of application after mortar deposition in a time frame of up to 200 min. This firmly positions automatically applied helical reinforcement as a viable method to reinforce 3DCP structures.

1. Introduction

The need for increased productivity, sustainability, safety and quality is driving the construction sector towards digital solutions, also known as a digital transformation towards Construction 4.0 [1]. To achieve this, the research and development of Digital Fabrication processes has exponentially grown over the past decade, illustrated through new large-scale projects being realized by private companies and universities on a global level [2]. One of these technologies is 3D concrete printing (3DCP), where concrete layers are deposited on top of each other with no need for formwork [3,4]. While the outlook for 3DCP is promising, there is also a multitude of obstacles that need to be overcome – one of which is the integration of reinforcement [5,6]. Developing viable reinforcement methods for printed structures is essential to move this technology to the next level [7].

It is common knowledge that concrete has a high compressive strength and a low tensile strength, which means for most load-bearing structures, concrete has to be reinforced against tensile and shear forces to achieve ductility. Perhaps the most instinctive solution, to apply conventional rebar, is not compatible with 3DCP structures, due to the differences in the manufacturing process; e.g. deposition of concrete taking place before rather than after the placement of reinforcement.

Some results have been published regarding the bond between printed concrete and conventional reinforcement bars. Linearly pushing a conventional bar inside concrete post printing seems to result in varying bond strength, with significantly reduced bond properties at the insertion side of the structure [8]. This was further confirmed by another research, where the creation of air voids and subsequent low bond and mechanical performance was reported, when placing reinforcement inside shotcrete 3D printed layers by a direct linear insertion method [9]. Placement by screwing has been presented as a potential solution to the aforementioned problems, as the helical geometry together with the introduction by combined translation-rotation overcomes the problem of reduced compaction around the reinforcement. In [9] it was reported that inserting a reinforcement bar by applying a screwing motion resulted in a significantly higher bond strength than with linearly

---

* Corresponding author.
E-mail address: l.hass@tue.nl (L. Hass).

https://doi.org/10.1016/j.conbuildmat.2022.129228
Received 20 June 2022; Received in revised form 15 September 2022; Accepted 16 September 2022

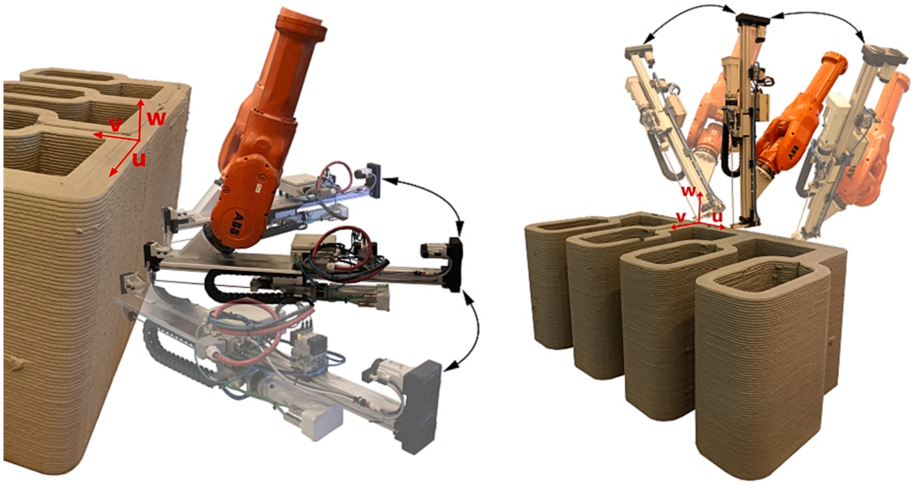

Fig. 1. Illustration of u-, v- and w-directions in extrusion-based 3D printed concrete together with the Automated Screwing Device.

inserted bars. A previous practically simultaneous study by the current authors on the placement of helical reinforcement by a screwing motion, confirmed this [10]. However, little is yet known about the actual bond characteristics of such reinforcement. It may be expected that it depends on a range of parameters such as print mortar viscosity, yield stress, transverse confinement, placement time post deposition, placement speed and reinforcement geometry and material. In this paper, we have studied the bond characteristics as a function of insertion time and screw geometry, by comparing the results of confined pull-out tests, supplemented by analysis of micro-computed tomography (μCT) scans.

2. Theory

2.1. *State-of-the-art*

There is a multitude of different reinforcement concepts that have been introduced to reinforce 3D concrete printed structures [50] in different direction of the printed layer as described in [51] and shown on Fig. 1. Some of the solutions have been applied in large scale structural application, while others are still in a conceptual phase. Regardless, a one-size-fits-all solution has not yet been developed.

In the early adoption of 3DCP, the printed structure was used as lost formwork, where traditional reinforcement was placed inside and then filled with cast concrete [11]. Traditional reinforcement has also been placed horizontally between printed layers and vertically through the layers, to reinforce structures similarly to traditional construction [8,12,13]. Alternatively, applying reinforcement post printing by prestressing externally [14] or through the structure with tendons [15] has shown potential.

Perhaps one of the most promising reinforcement concepts in the u-direction is the cable reinforcement, where a high strength steel cable runs off a spool into the concrete layer, without limiting the form freedom [16]. Similarly, a flow based pultrusion method has been used to insert multiple lines of basalt fibres into a printed layer [17]. Additionally, mineral-impregnated carbon fibre (MCF) composites have also been used [18]. A step further from this is a mesh reinforcement concept, using galvanized steel wire mesh, that also runs off a spool, but now also reinforcing the w-direction as well [19]. Some of latest developments include reinforcement elements such as nails [20], staples [21] and screws [10]. A number of studies has also been done investigating the application of various fibres to improve material ductility [22–28]. Due to the process of 3DCP, most concepts suffer from high void content or not being validated on a large scale [38]. While multiple strategies are in development, a universal solution has not yet been found.

2.2. *Background*

While multiple large scale projects have been realized, their structural integrity has been achieved in traditional ways, referring to solutions used in unreinforced masonry structures or creating compression structures [5,45]. None of the integrated reinforcement concepts developed have been used as primary reinforcement on a large scale as of yet. This is an indication that regarding reinforcement strategies for 3DCP, there is a clear gap between developments and what is actually being applied on large scale structures.

The previous doesn't necessarily come as a surprise as there are multiple obstacles that need to be considered, before a reinforcement concept can be approved for a large scale application. Ideally, a suitable reinforcement strategy for 3DCP would fulfil all the structural functionalities and continuity as a reinforcement element, be applicable in multiple directions of the printed structure as shown on Fig. 1 (or fulfil structural functionalities in one direction, while not limiting the use of a different reinforcement concept in another direction), not limit the geometric freedom of the 3DCP technology and work simultaneously with the printing process. Thus, the considerations can be divided into two, where on one hand the reinforcement concept is evaluated based on its practical application merits mentioned previously and on the other hand on available testing methodologies to appropriately evaluate structural integrity in printed structures.

Traditional reinforcement concepts are initially evaluated on small scale, in most cases presenting the interaction between reinforcement and the matrix in the form of bond strength. Relevant standards list numerous properties that affect bond strength between concrete and steel, e.g. in *ACI* 408R-03 [30], concrete cover, concrete properties, confinement reinforcement, casting direction, bar diameter, aggregate strength, aggregate quantity, transverse pressure and others are listed. To evaluate and compare bond properties between different test setups have been proposed [30]: pull-out specimen, beam-end specimen, beam anchorage specimen and splice specimen. While the proposed specimens are applicable for traditional reinforcement concepts, a code to characterize the bond strength between 3D printed concrete and reinforcement however, does not exist.

Because of the simplicity and ease of application, most researchers have modified the direct pull-out test [8,9,12,47] to describe the bond properties of discrete reinforcement elements in 3D printed concrete. To produce these test elements, where the embedded reinforcement is inside printed concrete, a multi step process is required, where the reinforcement is placed inside printed concrete and subsequently placed inside a formwork and cast to size, resulting in a confined pull-out specimen.

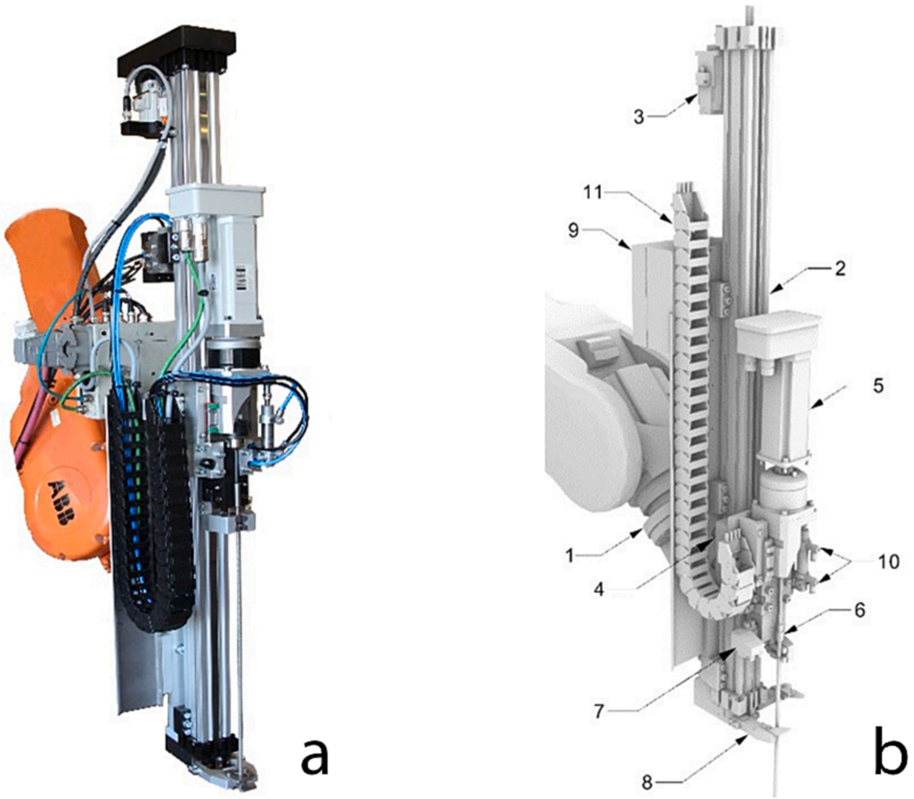

Fig. 2. Automated Screwing Device.

The authors previously tested the helical reinforcement in pull-out, where the reinforcement element was placed directly inside printed layers, without any additional confinement from cast concrete [10], which resulted in splitting failure in concrete, without any slip. To evaluate the helical reinforcement method better and to further investigate the gap between confined and unconfined pull-out tests, direct pull-out tests according to RILEM RC6 [29] were performed in the current study.

3. Helical reinforcement method

In this paper further investigation is done into the helical reinforcement method, by investigating the bond characteristics as a function of insertion time. Based on previously published results [10], an experimental program was comprised using a gantry type 3D concrete printer and an ABB robotic arm for reinforcement placement. The bond properties were investigated by comparing pull-out tests with different printable mortars, reinforcement geometries and placement times, supplemented by analysis of μCT-scans.

In traditional reinforced concrete with ribbed bars, up to 90 % [31] of the maximum pull-out resistance is generated by dilatancy, which is a result of the mechanical interlock between the ribbed surface merged in concrete. The tight packing of the matrix around the reinforcement is generally achieved by vibrating the concrete shortly after it is cast on top of the reinforcement, or using self compacting concrete. For printed structures, this problem can be overcome by applying a screwing motion to a helical reinforcement.

The concept entails a linear reinforcement element with a continuous helical surface being introduced into the fresh concrete some time after deposition, by a synchronized translational and rotational motion along the longitudinal axis of the reinforcement. Screwing into fresh printed mortar has a distinct difference to conventional screwing, in the way the material responds to the screwing motion. To apply helical reinforcement, the translational and rotational movement need to be aligned, i.e. during one 360° rotation, a translation equal to the helix lead should be performed. Normally (e.g. when screwing in timber), only the rotation needs to be applied by external force. The translational pull-in movement is ‘automatically’ generated by the resistance of the matrix material. The fresh printed mortar, however, is initially too weak to generate such resistance. Applying only a rotation would just lead to the helical reinforcement turning around but not entering into the mortar. Thus, the translational-rotational movement needs to be externally controlled. The rotation has to be combined with a translational push inward. In the experiments presented in this study an industrial robot arm robot is used, together with a custom developed end-effector (detailed below), to control the placement of the reinforcement as described previously.

The helical reinforcement method makes use of the pliant state of the fresh mortar after deposition. After deposition, the mortar will start to build up strength and stiffness, initially due to structuration [32] and later through hardening. This means that there will be a time window in which the method can be applied, since the deposited material will become too hard at some point to drive the helical reinforcement in without damaging either the reinforcement or the concrete. The time window will be highly material dependent, since printable mortars have considerably varying structuration rates and setting times. This will set boundary conditions on the design, such as layer length, object height and printing speed.

To evaluate the feasibility of inserting reinforcement by a screwing motion, an automated placement system was developed that would guarantee a controlled placement method and work simultaneously with the printing process.

The Automated Screwing Device (ASD; patent pending [49]), shown in Fig. 2a, is a robotic end-effector that is capable of introducing bar like elements with a helical geometry or helical surface (e.g. screws) into pliable materials, such as printable mortars before their initial setting time, by generating a controlled screwing motion.

The ASD is attached to a commercially available robotic arm, which positions the ASD to a desired global placement location (e.g. in the

Table 1

Mortar data as provided by their respective manufacturer datasheets [33,34], as obtained from additional characterization experiments, and as taken from other research.

	Weber 3D 145–2	Italcementi i.tech 3D N
Product datasheet data		
Largest Aggregate size	1 mm	2 mm
Density	2200 kg/m^3	2150 kg/m^3
Compressive Strength (28 days)	45 MPa	60 Mpa
Water amount by mass	16.5 %	16–18 %
Workability	120 min open time (unspecified); setting time, initial ≤ 220 min (according to EN 196-3 [53])*	28 min workable life (according to EN 1015–9 [54]); setting time, initial ≤ 150 min; final ≤ 200 min (according to EN 196–3 [53])
Experimental results characterization		
Compressive strength (average at 28 days according to NEN-EN 196-1 [52], with relative standard deviation between brackets)	Set WO: 55.4 MPa (1.79 %) Set WG: 58.9 MPa (2.97 %)	Set IO: 40.7 MPa (3.78 %) Set IG: 47.9 MPa (2.64 %)
Flexural bending strength (average at 28 days days according to NEN-EN 196-1 [52], with relative standard deviation between brackets)	Set WO: 4.23 MPa (14.6 %) Set WG: 6.55 MPa (5.39 %)	Set IO: 7.58 MPa (3.76 %) Set IG: 7.64 MPa (5.21 %)

* not given in the product data sheet [33], but taken from previously published research [44]

vicinity of the printed structure). With this global placement of the ASD, the insertion point and direction are defined for the helical reinforcement element. Subsequently, the ASD performs the local placement of the reinforcement element, i.e. introduction into the substrate (e.g. printable mortars). The application potential of the ASD has been discussed in [39].

Parts of the ASD are shown on Fig. 2b. The ASD is connected to the robotic arm by the mounting bracket (1). The main parts of the ASD are a sliding unit (4) which can be moved along a guide rail (2) by operation of motor unit 1 (3). Attached to the sliding unit are the motor unit 2 (5) and the top gripper (7). The motor unit 2 (5) is equipped with a connection bit (6), which is controlled by a pneumatic actuator (10). Also attached to the guide rail (2), is the bottom gripper (8). At the back of the device is an electrical box (9) and a cable protection system (11).

4. Experimental program

The experimental program included four distinct production sets with two different reinforcement geometries (original and grinded) and two distinct mortars (Weber 3D 145-2 and Italcementi i.tech 3D N). The sets were therefore named set WO (Weber 145-2 combined with original reinforcement), set IO (Italcementi i.tech 3D N combined with original reinforcement), set WG (Weber 145-2 combined with grinded reinforcement) and set IG (Italcementi i.tech 3D N combined with grinded reinforcement).

4.1. Mortars

Two different commercially available printing mortars were used: Weber 3D 145-2 and Italcementi i.tech 3D N [33,34]. A summary of available data has been provided in Table 1.

Further experimental work was performed to characterize the mortar properties. Three-point flexural bending tests were done conform NEN-EN 196-1, using a CONTROLS multipurpose compression-flexure cement testing frame. The test was performed on beams with dimensions of 40 × 40 × 160 mm and with a load rate of 50 N/s. Three beams were produced from each set of pull-out specimens, i.e. 12 in total (see Section 4.3). After flexural testing of the specimens, the 40 × 40 mm cross section of the 24 remaining halves were subjected to a compression test according to NEN-EN 196-1, at a load rate of 1000 N/s. All specimens were tested at an age of 28 days. The results of both tests are included in Table 1, and presented in Fig. 3a and 3b.

Remarkably, the Weber mortar was significantly stronger in compression than indicated in the product data sheet, while the Italcementi mortar, on the other hand, was quite a bit weaker (compare sets WO and WG to sets IO and IG).

In contrast, the flexural strength of the Italcementi mortar was higher than that of the Weber mortar. Considering the compressive strength was lower, this should not be attributed to a supposed higher binder content (note the actual composition is not disclosed by the suppliers), but rather to the fibre content (although not explicitly intended for structural purposes and of which fibre content and type are not indicated in the official data sheets). It is furthermore noted that the flexural strength of the Weber mortar deviated noticeably between sets WO and WG.

Both mortars have also been subjected to an ultrasonic wave transmission test (UWTT), in accordance to NEN-EN 12504-04, previously applied to printable mortars [44]. The results are shown in Fig. 4a for the 0–200 min time frame, and in Fig. 4b for the 0–80 h time frame.

4.2. Reinforcement

As reinforcement, cold-rolled wire, full thread zinc coated carbon steel screws were used, article number 1201010803005, manufactured by SPAX International GmbH. Two different reinforcement geometries were used in this research, the original screw and a grinded down version. The geometries are illustrated in Fig. 5. In addition, the tip of

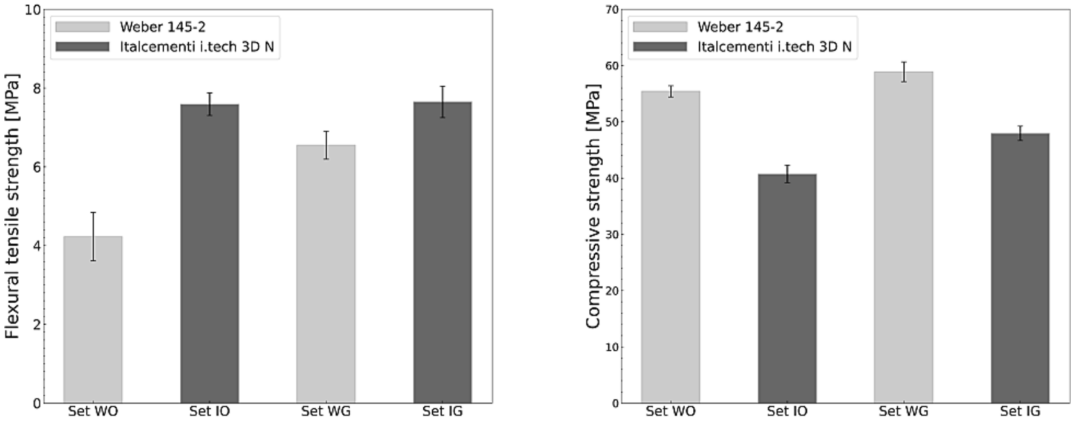

Fig. 3. a and b. Flexural bending strength (a, left) and compressive strength (b, right), for the printed mortar of each set.

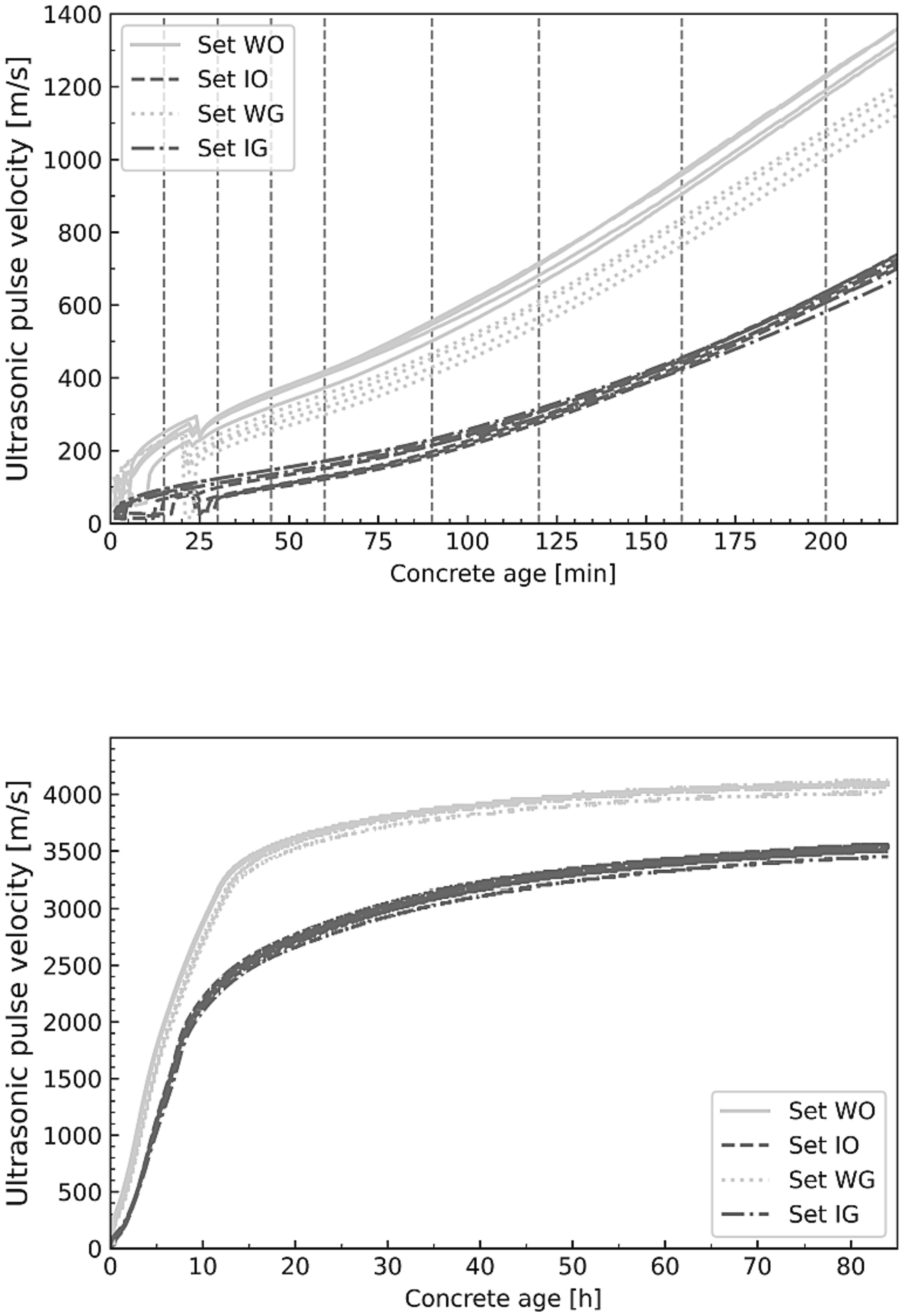

Fig. 4. and b. Ultrasonic pulse velocity measurements for the printed concrete of each set, where the vertical dashed lines indicate the reinforcement insertion time stamps for the first 200 min (a, top) and for 80 h (b, bottom).

the reinforcement was grinded to a cone, smaller than the rest of the reinforcement, in order for it not to affect the bond properties during placement.

It should be noted that these screws are designed to be used in load-bearing timber structures either for connecting members or as tensile and compressive reinforcement perpendicular to the grain direction. Because of this, the reinforcement geometry and material are not optimized for 3DCP, but was rather chosen due to its length to diameter ratio and product availability.

According to the European Technical Assessment [35], the screws have a characteristic tensile strength of $F_{t,k} = 17$ kN. Additional tensile tests, performed for the current study according to ASTM A370 on 5 specimens (original geometry, non-grinded), globally supported this value. The tests, performed on an Instron 250 kN test rig equipped with a non-contact video extensometer at a loading rate of 0.5 mm/min, yielded approximately bi-linear force–displacement diagrams (as expected from cold-rolled steel), with an average yield load of 18.7 kN (range: 18.4–19.1 kN) and an average ultimate load of 22.3 kN (range: 22.0–22.7 kN). Assuming a net diameter of 5 mm, this corresponds to a yield strength of 950 N/mm^2 and ultimate strength of 1136 N/mm^2. The average axial strain at yield load is 0.5 %, while increasing to 1.8 % at maximum load.

4.3. *Print process and sample preparation*

The direct pull-out test [29] is a test to evaluate bond properties between reinforcement and matrix. Because of the particularities of the production process of 3DCP and the fact that insertion of the

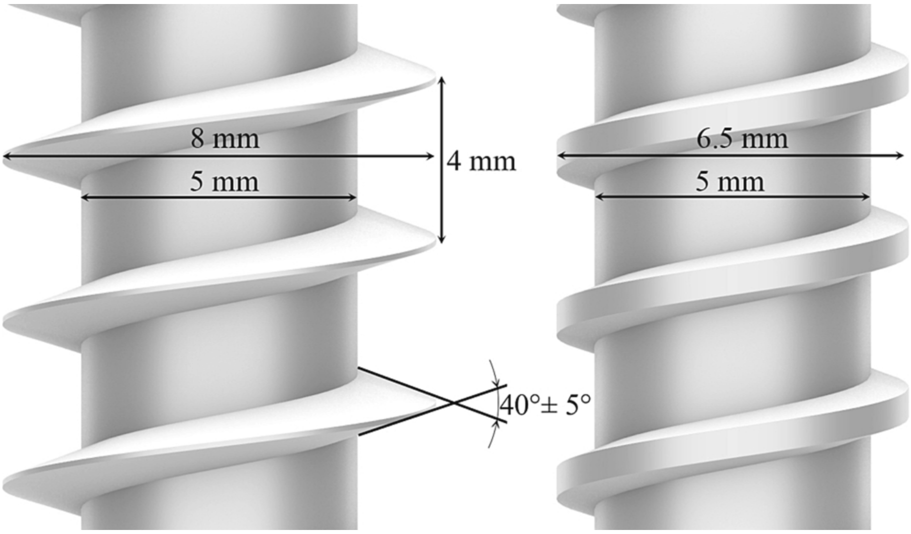

Fig. 5. Geometries of the used reinforcement with nominal dimensions – original (left) and grinded (right).

Table 2
Description of produced sets and conditions in laboratory. Each set comprised 5 samples for pull-out and 1 for μCT-scanning.

Set name	Mortar	Reinforcement type	Time stamps [min]	Lab air temperature [°C] and relative humidity [%]
WO	Weber 145–2	Original	Cast, 0, 15, 30, 45, 60, 90, 120, 160, 200	21.7/40.5
IO	Italcementi i. tech 3D N	Original		21.2/46.5
WG	Weber 145–2	Grinded		20.4/49.5
IG	Italcementi i. tech 3D N	Grinded		21.4/42.5

reinforcement would have to happen after concrete deposition, the production of the specimens had to be altered in comparison to the standard approach.

The two reinforcement geometries (original and grinded) were applied to the two mortars at 9 different time intervals after printing (hereafter: time stamps). In addition, samples were prepared where concrete was cast around a preplaced helical reinforcement element. The samples were designated as time stamp: cast. For every other time stamp, one extra printed specimen was produced for μCT scanning. In total 5 samples were prepared per one configuration, resulting in 200 pull-out and 20 μCT scan specimen.

For printing, the 3DCP setup in Eindhoven University of Technology (TU/e) [31] was used, which consists of a 4 degree-of-freedom gantry robot and a M-Tec Connect mixer-pump. The printing speed was 5000 mm/min and the layer offset 9.5 mm. The description of each printed sets and laboratory conditions during printing can we found in Table 2. Salad Slicer [36] plugin in Rhineceros Grasshopper was used to program the used printpaths in G-Code.

First, the part where reinforcement would be embedded in was printed, which consisted of 9 straight printed sections, each section with a total dimension of 40 × 60 × 2000 mm. Each straight section represented a time stamp when reinforcement placement would take place

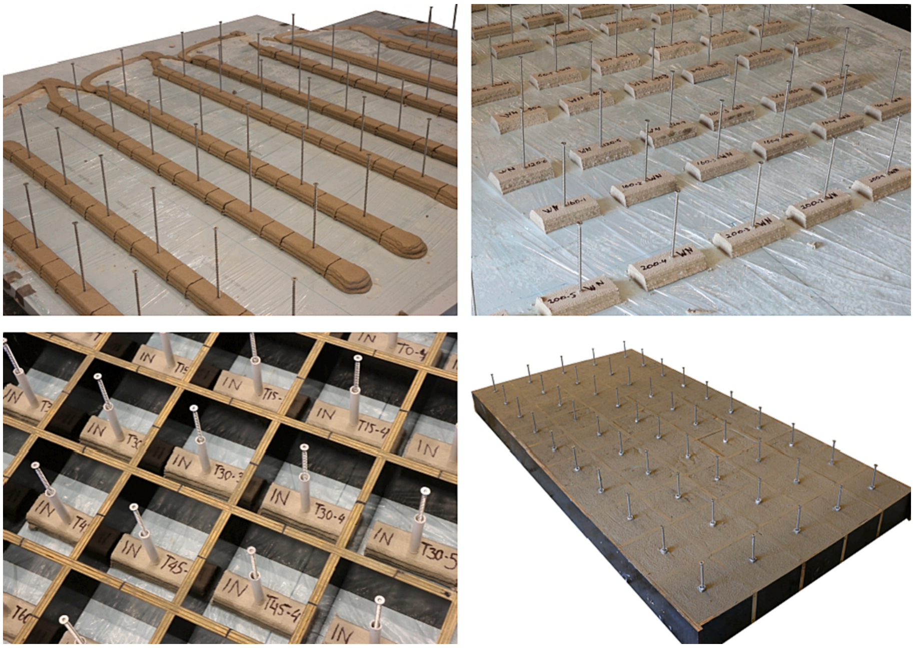

Fig. 6. Steps of the production process for one set.

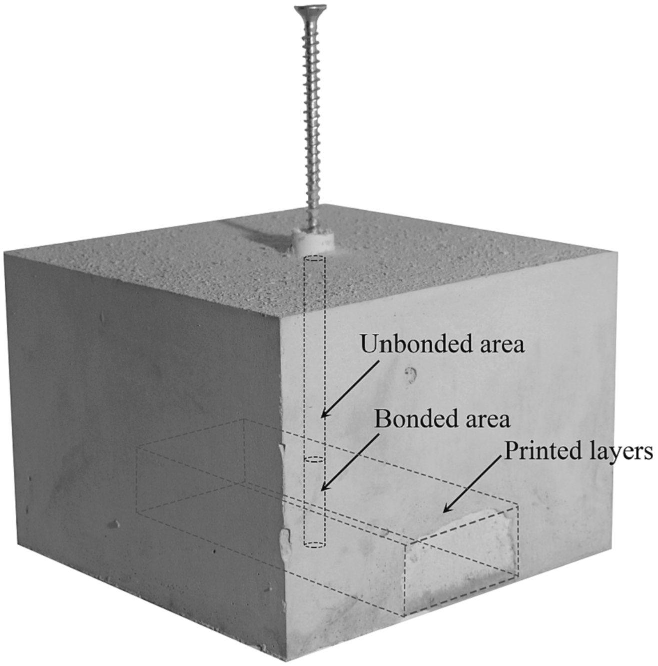

Fig. 7. A pull-out specimen.

after initial layer deposition. The chosen time stamps were chosen in a range expected to be relevant for 3DCP, up to approximately the initial set time. They were: $t = \sim 0$ (as soon as possible post printing); 15; 30; 45; 60; 90; 120; 160; 200 min after initial layer deposition. The chosen number in the abbreviation of the time stamps is an indication when the reinforcement was placed, with a deviation of ±4 min, due to the combination of the placement and printing process. The exact placement times are measured from the beginning of the 3rd layer deposition of each section, to the beginning of the reinforcement placement. The placement of an individual reinforcement element took 10 s. The exact placement times are presented in Annex A. As reference case, the cast version was produced at the same time, in a separate formwork, where the reinforcement element was pre-placed in the center of a 40 × 60 × 200 mm mold before pouring concrete around it and subsequently vibrating on a vibration table.

In order to fully embed the reinforcement and to accommodate for the displacement measurements during pull-out tests, the layers were printed on top of an XPS foamboard and the vertical reinforcement subsequently screwed through in the middle of the layer using the ASD, penetrating through the layers and into the pliable board, resulting in a bond length of 40 mm. The ASD was used to place the reinforcement inside printed layers with an RPM of 150, which, based on the lead of the reinforcement, resulted in a translational movement of 10 mm/s. The ASD is controlled by a custom developed script in RAPID code ran in the ABB controller. Robot Components plugin [37] in Rhinoceros Grasshopper was used to generate the RAPID code that controlled the ABB controller.

After the reinforcement had been placed, the sections were cut into 40 × 60 × 200 mm specimen and covered with plastic foil for 24 h. Subsequently, a plastic sleeve was placed around the top part of the reinforcement element for debonding purposes. The specimen were placed in 200 × 200 × 160 mm moulds and filled with cast concrete (of the same composition as the printed material) and covered in plastic for another 24 h, before demoulding and placing under water for 26 days. The steps of the production process are illustrated in Fig. 6, with the final pull-out specimen illustrated on Fig. 7.

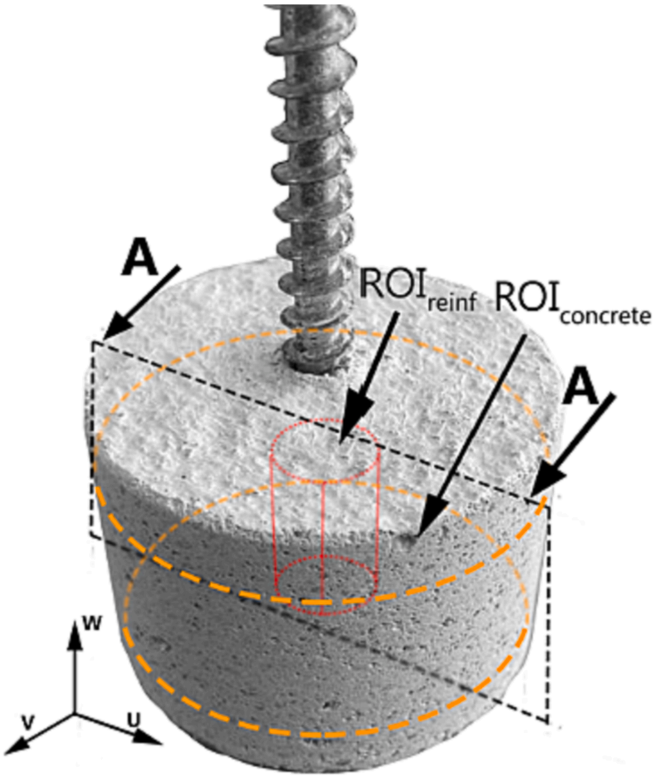

Fig. 8. A specimen for μCT, with region of interest around the reinforcement ROI_{reinf} and inside the printed specimen $ROI_{concrete}$, and section A-A.

4.4. *Microcomputed tomography (μCT) scanning*

To better understand the time dependent bond properties in relation to the reinforcement insertion, without damaging the bonding zone, μCT scanning was used to quantify the air void content in the immediate vicinity of the helical reinforcement, in comparison to the air void content further away from.

In μCT images, different materials can be segmented based on the greyscale intensity of each pixel, which corresponds to the local mass density. The pixel values in a 8-bit grayscale range from 0 to 255, where 0 corresponds to the black colour and 255 corresponds to white colour, with all other shades of gray being in between. To segment the different materials from one another, a thresholding method is used where particles between a minimum and maximum grayscale values are selected and the rest is disregarded. Because of the steel reinforcement reflecting a significant amount of artifacts on the scans, a manual thresholding method is used, i.e. a fixed minimum and maximum is selected for all images and the results are compared.

In the current study, a Phoenix Nanotom μCT-scanner was used at Delft University of Technology. A voltage of 150 kV, a current of 210 μA and an open time of 500 ms was applied. The scanning resolution was 2284 × 2284 pixels, with a voxel size of 0.0275 × 0.0275 × 0.0275 [mm]. During scanning, a picture was made every quarter of a degree with respect to the vertical axis (i.e. the longitudinal direction of the helical reinforcement). In total 1440 images were taken. The images were reconstructed into a 3D volume using VGSTUDIO software [40].

These images were then exported to ImageJ [41] and post-processed to quantify the air content in all scanned sets. A 5x5x5 median filter was used over the entire 3D volume to reduce noise artifacts originating from the steel reinforcement. To make the images binary, auto local threshold was applied, using the Phansalkar thresholding method [42]. The required parameters $k = 0.25$ and $r = 0.5$ for computing the threshold were selected by trial and error, comparing the location and size of air

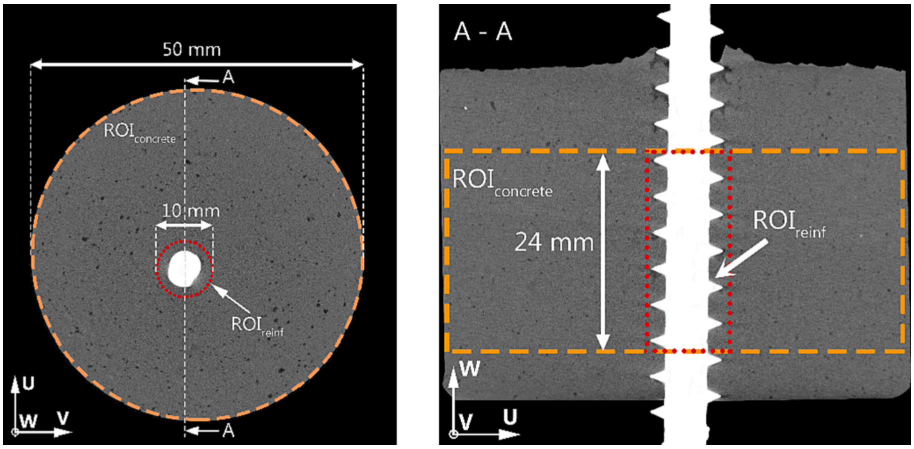

Fig. 9. Image of a µCT scanned cross-section (left) and a section A-A (right).

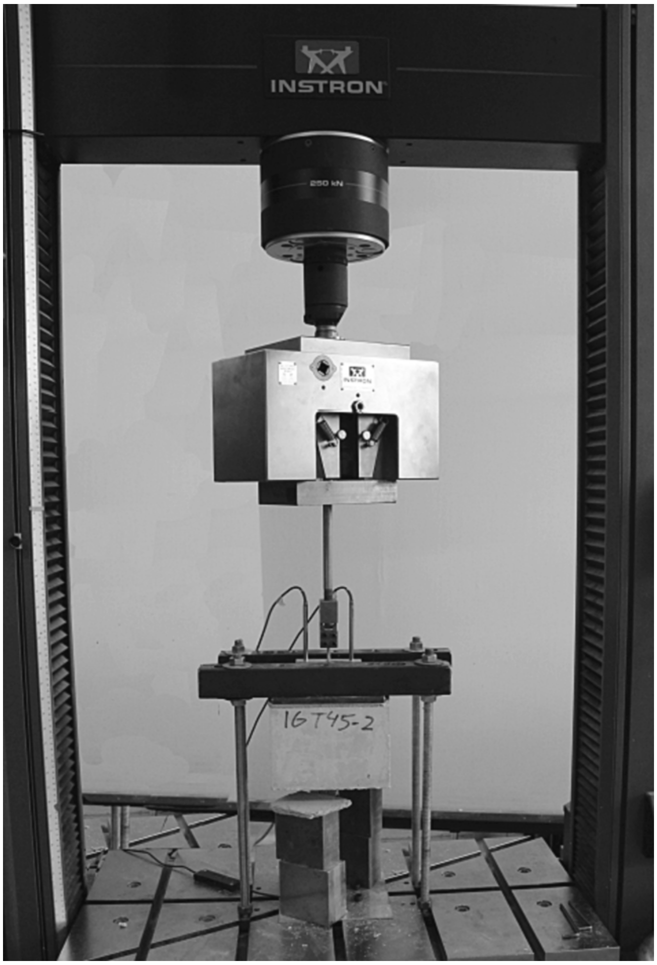

Fig. 10. Direct pull-out test setup.

voids to the original images. Two different volumes inside the specimen were selected as region of interest – region of interest around the reinforcement (ROI_{reinf}) and region of interest inside the concrete $(ROI_{concrete})$, shown in Fig. 8 and Fig. 9. The two volumes are compared to each other based on their air content per volume. The volume height was selected to be 24 mm (twice the size of the diameter of volume ROI_{reinf}) and located in the middle of specimen.

Scans were done on one specimen from the following time stamps of each set: ~t0, t60, t120, t200 and cast specimen. The void content for two different regions of interest (ROI) were calculated. $VC_{ROI_{reinf}}$, Eq. (9), represents the air void content per volume in the vicinity of the reinforcement, while $VC_{ROI_{concrete}}$, Eq. (10), represents the air void content per volume for the rest of the specimen, excluding the volume of ROI_{reinf}.

$$VC_{ROI_{reinf}}[\%] = \frac{\nu_{voids,ROI_{reinf}}}{\nu_{ROI_{reinf}} - \nu_{reinf}} \tag{9}$$

Where:

$\nu_{voids,ROI_{reinf}}$ –volume of air voids inside.ROI_{reinf}

$\nu_{ROI_{reinf}}$ – volume of.ROI_{reinf}

ν_{reinf}– volume of the reinforcement.

$$VC_{ROI_{concrete}}[\%] = \frac{\nu_{voids,ROI_{concrete}}}{\nu_{ROI_{concrete}}} \tag{10}$$

Where:

$\nu_{voids,ROI_{concrete}}$ –volume of air voids in.$ROI_{concrete}$

$\nu_{ROI_{concrete}}$ – volume of.$ROI_{concrete}$

4.5. Pull-out tests

Direct pull-out tests were done according to RILEM RC6, using an Instron 250 kN testing rig. Displacement control was selected to capture the ultimate load and post-peak behaviour with a displacement rate of 1.5 mm/min. A layer of softboard was placed between the support plate and the specimen, to distribute loads better and account for any uneven surface. The pull-out load is applied at the top of the reinforcement, where it is clamped to the testing rig by a hinged joint, to remove potential bending moments resulting from the inaccuracies of the reinforcement placement. A specimen placed in the testing rig can be seen in Fig. 10.

The relative displacement was measured from the loaded end by two Linear Variable Differential Transducers (LVDT). The LVDTs were fixed 60 mm apart, on either side of the reinforcement. The core of the LVDT was placed on top the confined specimen, through the supporting plate and softboard.The average of the two LVDT was recorded, in the case of the reinforcement being not completely straight. At the free end, slip was measured in the same manner, by a single LVDT.

The bond strength $\tau_{b,max}$ was calculated, assuming a uniform stress distribution along the embedded length, according to Eq. (11):

$$\tau_{b,max} = \frac{F_{max}}{\pi \bullet \varnothing \bullet l_b} \tag{11}$$

With: F_{max} = maximum load, $\varnothing$ = outer diameter of the reinforcement, l_b = bond length.

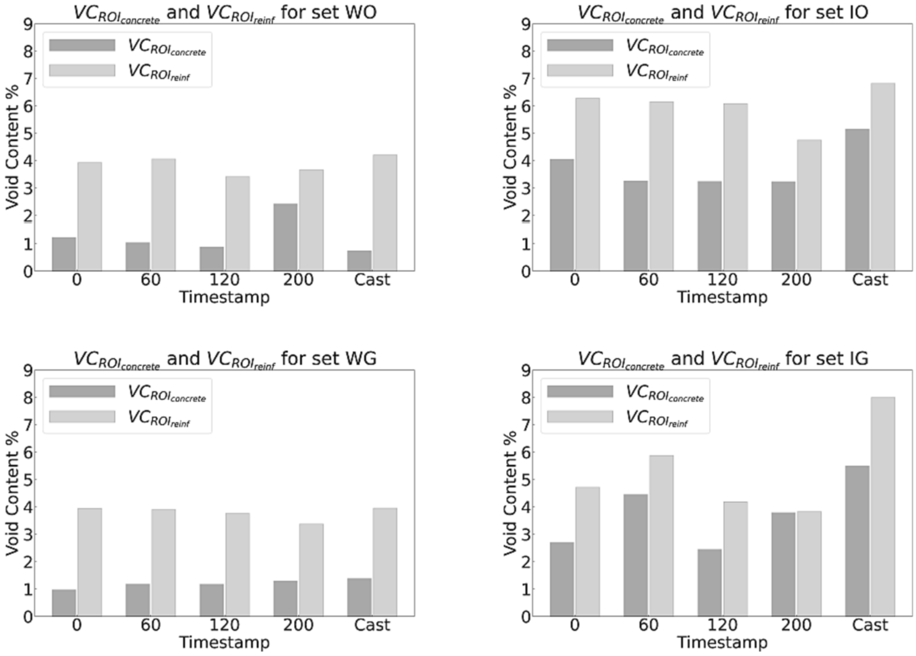

Fig. 11. Void content for all mixes.

Table 3
Air void content in the printed concrete at the region of interest for each timestamp.

Set nr.	Time stamp	$VC_{ROI_{concrete}}$	RSD	$VC_{ROI_{reinf}}$	RSD	$VC_{ROI_{diff}}$	RSD
Set WO	t0	1.23	15.89 %	3.93	6.55 %	2.70	9.78 %
	t60	1.04		4.06		3.02	
	t120	0.88		3.42		2.54	
	t200	1.35		3.66		2.31	
	μ t0-200	1.13		3.77		2.64	
	Cast	0.74		4.21		3.46	
Set IO	t0	4.05	10.13 %	6.27	10.60 %	2.22	23.36 %
	t60	3.26		6.14		2.88	
	t120	3.24		6.08		2.84	
	t200	3.23		4.75		1.52	
	μ t0-200	3.45		5.81		2.37	
	Cast	5.15		6.82		1.67	
Set WG	t0	0.97	9.99 %	3.94	6.02 %	2.97	12.57 %
	t60	1.17		3.9		2.73	
	t120	1.17		3.76		2.59	
	t200	1.29		3.37		2.08	
	μ t0-200	1.15		3.74		2.59	
	Cast	1.38		3.9		2.52	
Set IG	t0	2.7	24.35 %	4.71	16.66 %	2.01	18.55 %
	t60	4.45		5.87		1.42	
	t120	2.44		4.18		1.74	
	t200	3.78		3.82		0.04	
	μ t0-200	3.34		4.65		1.30	
	Cast	5.49		7.99		2.50	

5. Results and discussion

5.1. *μCT-Scans*

The air void content $VC_{ROI_{concrete}}$ and $VC_{ROI_{reinf}}$ for all printed sets are presented in Fig. 11 and Table 3. The Weber 3D 145–2 had an average air void content of 1.13 % in set WO and 1.15 % in set WG, over the time stamps t = 0 to t = 200 min. The air void content in the Italcementi i.tech 3D N was approximately-three times as high, measuring 3.45 % in set IO and 3.34 % in set IG on average.

As expected, the variations between the averages of the sets of the same material are small (compare sets WO with WG and IO with IG), but the relative standard deviation inside $ROI_{concrete}$ for all printed sets is between 9.99 and 24.35 %, even though all time stamp sections inside a set are produced as a continuous print and would therefore be expected to have a relatively small deviation. This variability may be caused by fluctuations in entrapped air, resulting from the mixing, pumping and printing process.

The air void content in the Weber mortar does not seem to be affected significantly by the print process (compare cast to printed specimens in sets WO and WG). In the Italcementi mortar, on the other hand, the air void content seems to be reduced slightly due to printing, which may be caused by pressure in the system prior to deposition (compare cast to printed specimens in sets IO and IG).

A first glance at the data may give the impression that the air void content reduces slightly at higher time stamps. However, this effect is not very consistently observed and too few data is available to draw conclusions with regard to this aspect.

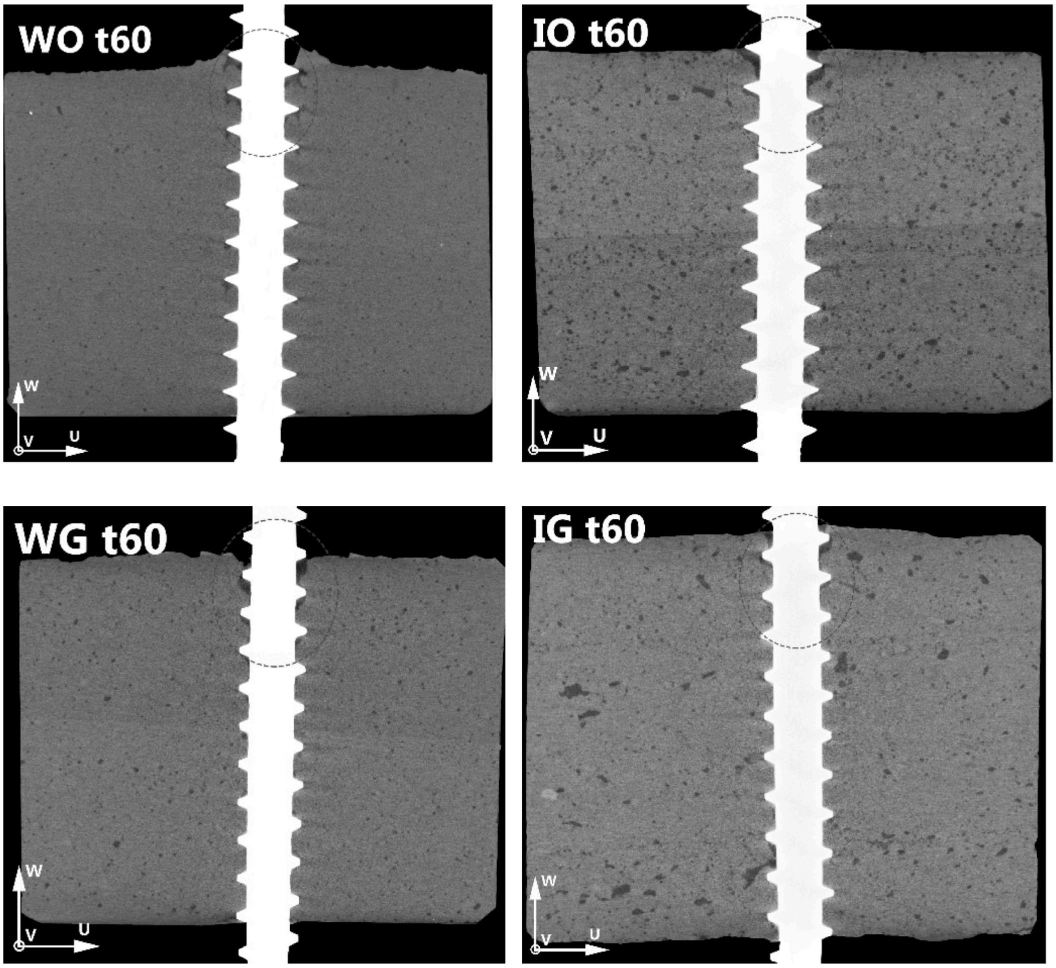

Fig. 12. µCT-Scan specimens with highlighted disturbed zone in the upper part of the specimen.

Similarly, the screw geometry (original versus grinded) does not show a clear effect. In the Weber mortar, the $VC_{ROI_{concrete}}$ remains practically unchanged (3.8 % vs 3.7 %), while in the Italcementi mortar a potentially significant reduction from 5.8 % to 4.7 % was found. Again here though, caution should be applied as to the general validity of this difference, considering the number of studied specimens.

$VC_{ROI_{diff}}$ is the difference between $VC_{ROI_{concrete}}$ and $VC_{ROI_{reinf}}$, and therefore represents the change in air void content caused by the insertion of the reinforcement by the ASD. For all sets, an increase in air void content was found in $VC_{ROI_{diff}}$. The increase in set WO and WG was 2.64 and 2.59 %-point respectively, while for set IO and IG it was 2.37 and 1.3 %-point (although this latter result is heavily influenced by the t = 200 specimen, which may be an outlier – ignoring this specimen would result in an average $VC_{ROI_{diff}}$ of 1.7 %-point).

It should be observed that a $VC_{ROI_{diff}}$ of several %-point was not only found for the printed specimens, but for the cast specimens too (varying between 1.7 and 3.5 %-point for set IO and set WO, respectively). As the screws have been pre-placed in these specimens (before casting), this means the difference may result from the screwing process, but does not necessarily have to.

Focusing now on the area where the reinforcement is inserted (Fig. 12), the scans show the mortar is significantly more damaged than the rest of the section. This can be explained by the inaccuracies of the reinforcement geometry, as the ASD calculates the placement parameters based on the nominal lead of the reinforcement. If the lead of a reinforcement element deviates during placement however, the reinforcement will start to push the material either up or down. The smaller the lead of the reinforcement, the more deviation. Fortunately, the inaccuracies in the geometry are minor and due to the increased

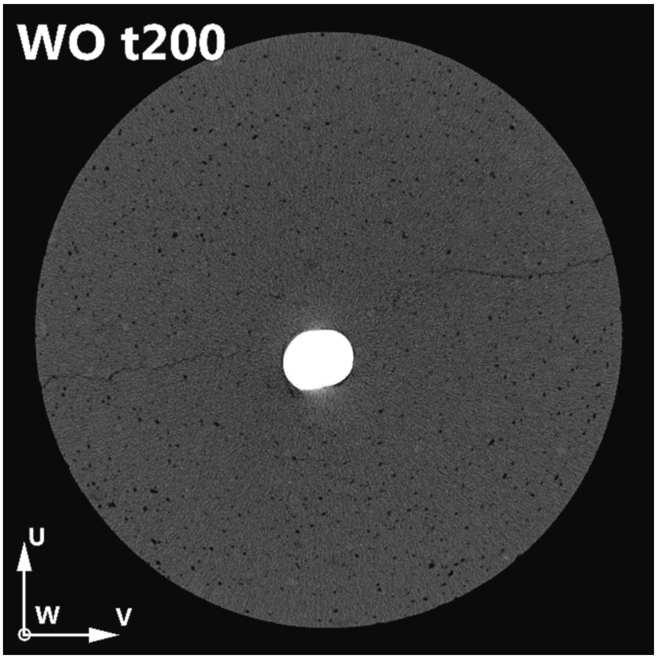

Fig. 13. Micro cracks seen in µCT-Scans for set WO, time stamp 200.

Table 4
Average peak load $F_{max,ave}$ in pull-out for every time stamp in each set, dominant failure mode (PO - Pull-out of reinforcement; YR - Yielding of reinforcement) and relative standard deviation RSD.

Set nr.	Time stamp	$F_{max,ave}$ [kN]	Dominant Failure	RSD [%]	Set nr.	Time stamp	$F_{max,ave}$ [kN]	Dominant Failure	RSD [%]
Set WO	t0	20.83	YR	2.49 %	Set IO	t0	18.45	PO	2.37 %
	T15	21.63	YR	1.28 %		T15	18.59	PO	1.84 %
	T30	21.32	YR	1.93 %		T30	19.56	PO	0.89 %
	T45	21.25	YR	0.68 %		T45	19.60	YR	1.11 %
	t60	21.19	YR	1.63 %		t60	19.63	PO	1.11 %
	T90	21.51	YR	2.31 %		T90	19.47	PO	1.83 %
	t120	21.22	YR	2.97 %		t120	19.23	PO	2.09 %
	T160	21.35	YR	1.99 %		T160	20.42	YR	2.06 %
	t200	21.06	YR	1.48 %		t200	20.59	PO	1.37 %
	t0-200	21.26		1.86 %		t0-200	19.50		1.63 %
	Cast	19.87	YR	2.63 %		Cast	15.73	PO	17.10 %
Set WG	t0	19.86	YR	1.69 %	Set IG	t0	21.23	YR	0.83 %
	T15	20.66	YR	4.51 %		T15	20.62	PO	0.93 %
	T30	20.98	YR	0.26 %		T30	19.27	PO	3.79 %
	T45	19.76	YR	1.94 %		T45	18.47	PO	2.96 %
	t60	20.79	YR	4.95 %		t60	18.40	PO	3.97 %
	T90	19.79	YR	3.65 %		T90	18.06	PO	1.29 %
	t120	20.55	YR	2.11 %		t120	19.58	PO	4.38 %
	T160	20.36	YR	0.60 %		T160	20.49	YR	1.75 %
	t200	19.97	YR	3.14 %		t200	20.78	YR	1.35 %
	t0-200	20.30		2.54 %		t0-200	19.65		2.36 %
	Cast	20.62	YR	3.57 %		Cast	16.55	PO	13.94 %

concrete confinement at deeper locations and the material not being fully hardened, this disturbance is not seen in the rest of the specimen. However, at the insertion location of the structure, this will have the biggest effect as there is no confining material around it and concrete is able to freely be pushed upwards.

In the specimen of set WO and set WG, t200 minutes, micro cracks were found (see Fig. 13). Similar cracks were not found in any other specimen. Cracking indicates that as a result of inserting a reinforcement element, and the equivalent displacement, the fracture strain of the concrete is exceeded, which is known to decrease over time, even in the fresh state [43,46]. The fact that this was observed in the Weber mortar, which has a higher open time and initial set time (see Table 1) and higher strain at maximum compressive strength (unpublished research) than the Italcementi mortar, may be explained by the lack of fibres. Although the micro cracks did not seem to affect the pull-out resistance in the confined pull-out test (see Section 5.2), their presence may indicate the maximum time stamp has been reached even though it is technically still possible to introduce the reinforcement with the ASD. Micro cracks should be avoided as they may initiate global cracking, particularly in unconfined geometries. Furthermore, they may reduce the structural durability due to penetration of moisture and chemicals, which instigate degradation of the reinforcement or mortar.

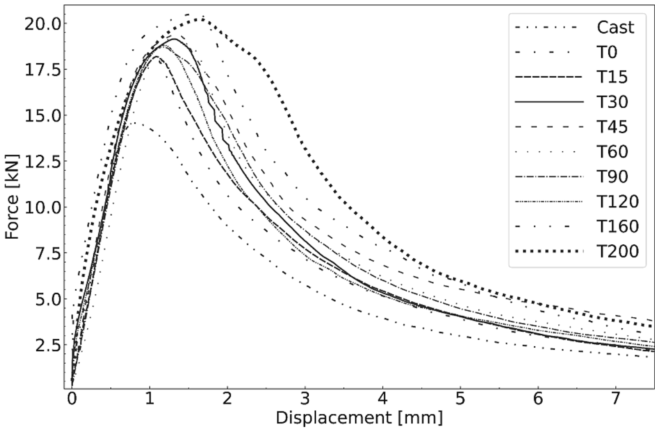

Fig. 14. Force-displacement graph for set IO.

5.2. Pull-out tests

200 confined direct pull-out tests were performed to describe the bond between printed mortar and placed reinforcement. Individual failure modes, placement times and bond stress are presented in Appendix A.

In Table 4 average peak loads for every time stamp in each set are presented, together with the dominant failure mode and the relative standard deviation.

5.2.1. Set WO and WG

In sets WO and WG, the expected slip out failure did not happen. All printed specimens in these sets failed by yielding of the reinforcement, without any visual observation of slip behaviour. This occurred at loads in between the yield and ultimate loads of the screws as determined during the tensile tests (see Section 4.2), i.e. the average failure load across all time stamps for set WO was 21.3 kN and 20.3 kN for set WG, while the yield strength of the screws was found to be $F_{y,ave} = 18.7$ kN, while the ultimate load $F_{t,ave} = 22.3$ kN. The corresponding bond stresses were $\tau_b = 21.2$ MPa and $\tau_b = 20.2$ MPa, respectively. Note that these values are very high compared to the characteristic bond stress of conventional reinforcement in e.g. a C50/60 concrete according to Eurocode 2 [48], which, assuming 'good' bond conditions, would yield only $f_{bk} = 6.5$ MPa (note that the 5 %-characteristic strength is lower than the experimental average, but the difference between conventional reinforcement and the helical reinforcement is nevertheless striking).

The experiments show that the confined bond strength over 40 mm embedment length in the Weber mortar is at least as high as the yield strength of the reinforcement. Due to the yielding failure mode, the effects of screw geometry and placement time could not be investigated further for this mortar. It could only be concluded that they did not reduce the bond strength below the yield strength of the reinforcement. The high bond strength should be attributed to the high mechanical interlock generated by the screw geometry, in combination with the mortar compressive strength.

On the other hand, the cast specimens in sets WO and WG gave a mixed results with regard to failure behaviour: in set WO, 4 out of 5 specimens failed by pull-out and in set WG, 2 out of 5 failed in pull-out (the rest by yielding). The average maximum loads were 19.9 kN and 20.6 kN, respectively, and thus in the same range as the maximum load in the printed specimens. The strength of the individual specimens could

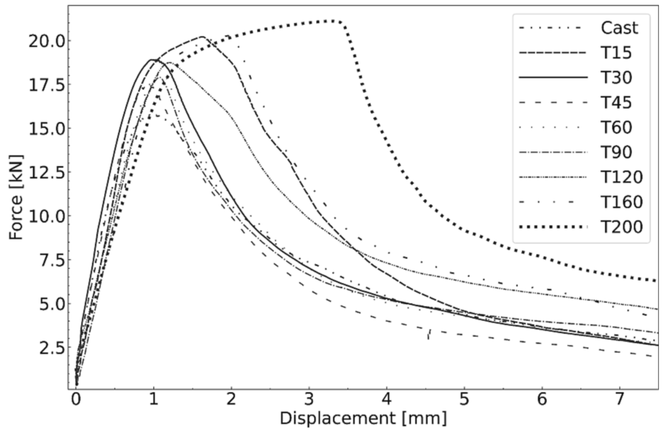

Fig. 15. Force-displacement graph for set IG.

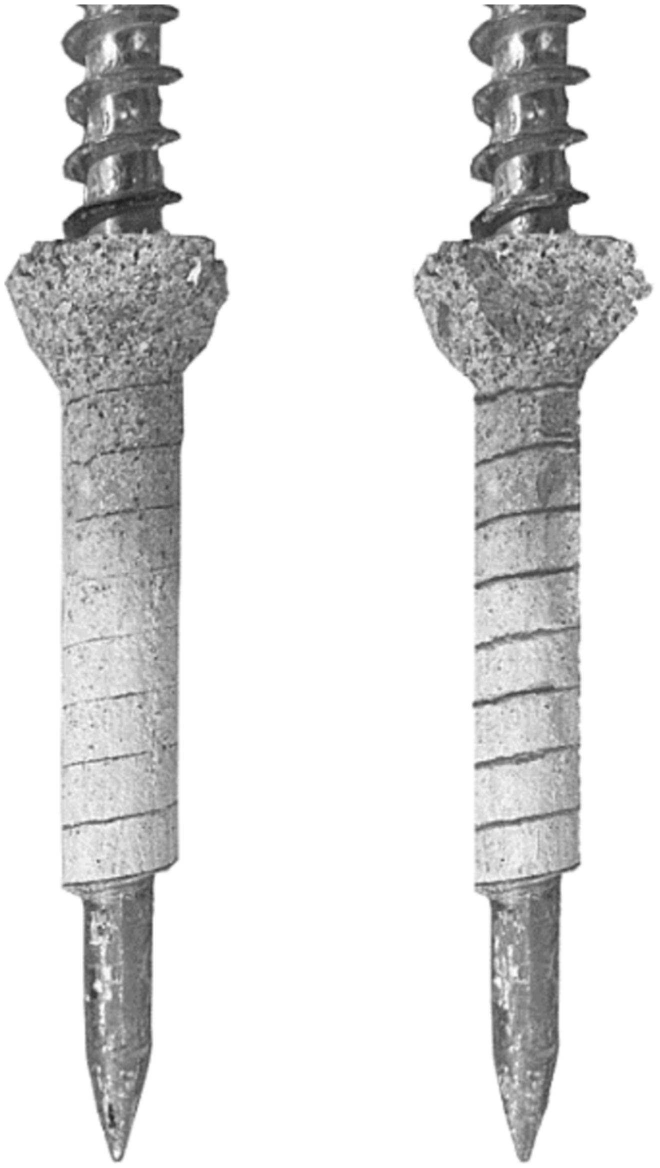

Fig. 16. Samples of pulled out reinforcement elements from IO (left) and IG (right).

not be correlated to the failure mode, i.e. the specimens failing in pull-out were not necessarily the weakest. Altogether, this seems to indicate that the limits for the two modes of failure are very close in this test set-up and specimen geometry, although preplacing a reinforcement with this specific geometry and casting print mortar around it with subsequently applied vibration, results in slightly worse bond properties when compared to placement by the ASD. The cause of this difference is not entirely clear, it could not be linked to a difference in air void content or visible cavities in the µCT-scans. It may be related to the microstructure of the flow front in the mortar that engulfs the screws in the cast specimens, whereas this is not the case in the printed specimens.

5.2.2. *Set IO and IG*

The load–displacement curves for sets IO and IG are represented in Figs. 14 and 15, respectively. Contrary to sets WO and WG, sets IO and IG failed predominantly by pull-out, with the exception of the t = 0 specimens of set IG, and mixed results for t = 30 and t = 45 in set IO (pull-out in 2 and 3 out of 5 specimens respectively). Although not entirely identical, the change in reinforcement geometry does not seem to effect the behaviour significantly. A linear response is found until approximately 90 % or more of the ultimate load. The stifness then gradually reduces, presumably due to microcracking. After the peak load, the remaining resistance decreases rapidly, as the fine-grained mortar generates little friction. Nevertheless, friction induced residual forces can be measured beyond 10 mm of pull-out displacement.

Fig. 16 shows an original and a grinded screw after pull-out, illustrating the typical fracture pattern obtained. Along most of its length, a cylindrical shear plane has formed along the tip of the screw helix. Near the top, the fracture converts to a cone shape due to the sleeve diameter being slightly wider than the screw itself.

For set IO the average failure load across all time stamps in printed specimens was 19.5 kN, with a corresponding bond stress of 19.4 MPa. In set IG, the average failure load across all time stamps in printed concrete was 19.7 kN, which corresponds to 19.6 MPa bond stress.

The cast specimens not only failed at considerably lower loads, average 15.7 kN and 16.6 kN for sets IO and IG, but also with a higher degree of scatter with relative standard deviations of 15.6 % and 19.1 %, while for the printed specimens this remains (well) below 5 % in all cases. It is remarkable that the difference between cast and printed specimens is much stronger with the Italcementi mortar than with the Weber mortar. The cause of this difference is unclear, and may perhaps be attributed to the flow properties of each mortar. However, it is relevant to observe that in both cases, the application of the reinforcement with the ASD into fresh mortar, results in a resistance that is higher than or at least equal to the resistance when the reinforcement is preplaced before casting.

The development of strength over increasing time stamps is illustrated in Figs. 17 and 18. In set IO a small gradual increase in bond strength can be seen for reinforcement placed at later time stamps, from 18.5 kN at t = 0 to 20.6 kN at t = 200. Such a trend was not found when looking at grinded reinforcement in set IG, where a moderate reduction in bond strength from 21.2 kN to 18.1 kN can be recognized until time stamp 90, after which the bond strength increases again to 20.8 kN at time stamp 200. No apparent reason for these trends and their difference was found either from the pull-out tests directly, or from consideration of the µCT scan results. Considering these contradicting trends and the consistent reinforcement yielding failure in sets WO and WG, an unambiguous relation between placement time and bond strength could not be derived. That being said, the change in pull-out resistance between the time stamps is small, 10,2% and 14,6% for sets IO and IG, respectively. Thus, it can provisionally be assumed that in a time frame up to 200 min after placement, the time stamp does not significantly influence the confined pull-out strength.

The results show that higher bond stresses for sets WO and WG than for sets IO and IG. Based on the flexural tensile strength of the respective mortars (4.22 MPa and 6.54 MPa for Weber mortar in sets WO and WG,

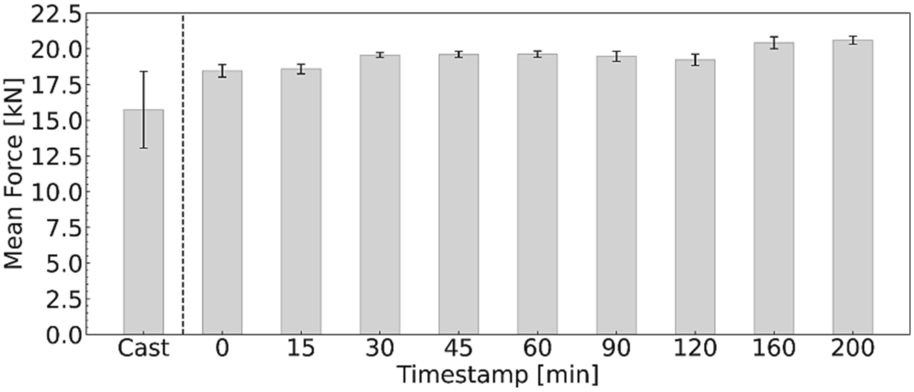

Fig. 17. Mean force distribution across all tested time stamps for set IO.

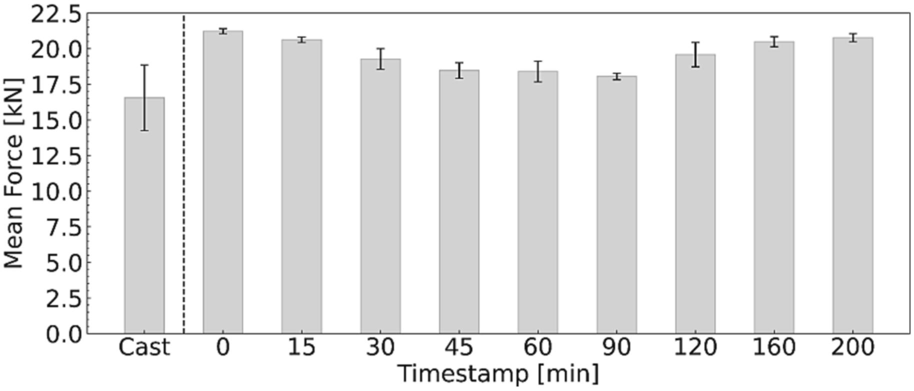

Fig. 18. Mean force distribution across all tested time stamps for set IG.

respectively, and 7.58 MPa and 7.64 MPA for Italcementi mortar in sets IO and IG), one might have expected an opposite trend. However, the failure in these specimens is governed mainly by the confinement, which in turn is correlated to the compressive strength of the respective materials, which was found to be higher for the Weber mortar (55.4 MPa and 58.9 MPa for sets WO and WG, respectively, while measuring 40.7 MPa and 47.9 MPa for the Italcementi sets IO and IG).

5.2.3. *Application potential*

Overall, the results clearly underline the potential of the concept of automatically placed helical reinforcement. The bond strength was shown to be very high. The automated, post-printing placement process itself was shown to be beneficial, leading to resistances as high as or higher than that of specimens with prepositioned reinforcement and cast mortar. This reinforcement method does not show significant effects of placement time until 200 min after deposition, for the 2 studied commercially available print mortars, either in terms of strength or ease of application. This would require reinforcement being applied less than once per 3 h. For a print speed of e.g. 10 cm/s and a layer height of 1 cm, this would correspond to a printed wall of 2 m high and more than 5.4 m long.

It should be recognized that the attained bond strengths are dependent on the level of confinement provided by the structure. In 3DCP applications, the use of relatively narrow layers may result in reduced confinement, and therefore earlier failure. This should be addressed in future research. Nevertheless, the presented results provide a strong basis for further development of the concept.

6. Conclusion

For the applied mortars in this study, the following conclusions can be drawn from the current work:

- A very high mechanical interlock can be achieved between reinforcement and mortar by automatically placing helical reinforcement into fresh printed mortars with the ASD, at least up to 200 min after deposition.
- Although higher values of air void content were found in the direct vicinity of the helical reinforcement, these could not be related to the placement method, nor to the resistance of the specimens, and therefore does not seem to have a noticeable influence.
- Besides the helical reinforcement geometry, the bond strength in the confined pull-out tests of this study was governed by the mortar compressive strength, but not by the flexural tensile strength.
- The change of the helical surface geometry by grinding to a lower height did not significantly influence the pull-out behaviour or resistance.
- The pull-out performance is not influenced significantly by the time of application after mortar deposition in a time frame of up to 200 min.
- The pull-out resistance achieved with post-applied reinforcement in printed mortar is at least as high (or considerably higher), than that obtained with pre-placed reinforcement in cast mortar.

Altogether, this firmly positions automatically applied helical reinforcement as a viable method to reinforce 3DCP structures.

CRediT authorship contribution statement

Lauri Hass: Investigation, Methodology, Writing – original draft. **F. P. Bos:** Conceptualization, Supervision, Writing – review & editing. **T.A. M. Salet:** Conceptualization, Supervision.

Declaration of Competing Interest

The authors declare that they have no known competing financial interests or personal relationships that could have appeared to influence the work reported in this paper.

Data availability

Data will be made available on request.

Acknowledgements

This study is part of a research project funded by Consolis SAS. Their support is gratefully acknowledged. Furthermore, the assistance of the staff of the Structural Engineering and Design Laboratory at TU Eindhoven and Faculty of Civil Engineering and Geosciences at TU Delft in the experimental program, is highly appreciated. Additionally, Kristjan Jaak scholarship fund provided by the European Regional Development Fund and Estonian government is acknowledged.

Appendix A. Placement times for all specimen, failure mode description, failure load and respective bond stress for all sets.

		Set WO				Set IO				Set WG				Set IG			
Placement time	Specimen Number	Exact Placement time [min: ss]	Failure mode	Force at failure [kN]	Bond stress at failure [MPa]	Exact Placement time [min: ss]	Failure mode	Force at failure [kN]	Bond stress at failure [MPa]	Exact Placement time [min: ss]	Failure mode	Force at failure [kN]	Bond stress at failure [MPa]	Exact Placement time [min: ss]	Failure mode	Force at failure [kN]	Bond stress at failure [MPa]
~t0	1	+1:32	YR	21.28	21.17	+1:20	PO	18.47	18.37	+1:52	YR	20.50	20.40	+1:52	YR	20.95	20.84
	2	+2:03	YR	20.69	20.58	+3:01	PO	18.40	18.31	+2:20	YR	19.50	19.40	+2:22	YR	21.10	20.99
	3	+2:37	YR	21.55	21.44	+3:29	PO	17.85	17.76	+2:51	YR	19.77	19.66	+3:02	YR	21.33	21.21
	4	+3:08	YR	20.52	20.41	+4:00	PO	19.21	19.10	+3:23	YR	19.77	19.66	+3:30	YR	21.31	21.20
	5	+3:39	YR	20.12	20.01	+4:30	PO	18.33	18.24	+3:57	YR	19.77	19.66	+4:22	YR	21.44	21.33
	6	+4:10	μCT scanned			+5:00	μCT scanned			+4:28	μCT scanned			+4:48	μCT scanned		
t15	1	+15:48	YR	21.74	21.63	+13:03	PO	18.20	18.11	+14:05	YR	18.93	18.83	+10:45	PO	20.86	20.75
	2	+16:19	YR	21.86	21.74	+13:37	PO	19.19	19.09	+14:41	YR	21.12	21.00	+11:32	YR	20.78	20.67
	3	+16:53	YR	21.33	21.22	+14:07	PO	18.60	18.51	+15:10	YR	21.70	21.59	+12:04	PO	20.38	20.27
	4	+17:24	YR	21.28	21.17	+14:38	PO	18.32	18.23	+15:38	YR	20.66	20.56	+12:33	PO	20.42	20.31
	5	+17:58	YR	21.96	21.84	+15:09	PO	18.62	18.52	+16:46	YR	20.91	20.80	+13:06	PO	20.67	20.56
t30	1	+31:21	YR	20.64	20.53	+31:28	PO	19.48	19.38	+31:45	YR	20.97	20.86	+28:51	PO	19.59	19.49
	2	+31:54	YR	21.37	21.26	+32:41	PO	19.59	19.49	+32:23	YR	21.07	20.96	+30:48	PO	19.92	19.81
	3	+32:27	YR	21.78	21.66	+33:13	YR	19.75	19.65	+32:54	YR	20.90	20.78	+31:38	PO	19.77	19.67
	4	+33:00	YR	21.12	21.01	+33:47	PO	19.27	19.17	+33:26	YR	20.97	20.86	+32:53	PO	19.17	19.07
	5	+34:27	YR	21.68	21.57	+34:20	YR	19.71	19.60	+33:56	YR	20.97	20.86	+33:29	PO	17.90	17.81
t45	1	+45:50	YR	21.37	21.26	+44:33	YR	19.52	19.42	+45:35	YR	19.82	19.72	+43:00	PO	19.35	19.25
	2	+46:27	YR	21.27	21.16	+45:07	PO	19.37	19.27	+46:07	YR	19.82	19.72	+43:41	PO	18.57	18.47
	3	+46:58	YR	21.20	21.09	+45:38	YR	19.44	19.34	+46:37	YR	19.07	18.97	+44:10	PO	18.11	18.02
	4	+47:28	YR	21.42	21.31	+46:08	PO	19.72	19.61	+47:07	YR	20.26	20.16	+44:41	PO	18.59	18.49
	5	+48:00	YR	21.01	20.90	+46:39	YR	19.97	19.86	+47:38	YR	19.82	19.72	+45:21	PO	17.72	17.62
t60	1	+59:50	YR	21.47	21.36	+61:0	PO	19.31	19.21	+60:48	YR	18.94	18.84	+57:40	PO	17.10	17.01
	2	+60:25	YR	20.57	20.46	+61:45	PO	19.55	19.44	+61:31	YR	21.47	21.35	+58:15	PO	18.53	18.44
	3	+61:00	YR	21.49	21.38	+62:16	PO	19.66	19.56	+62:04	YR	20.69	20.58	+58:49	PO	18.21	18.12
	4	+61:32	YR	21.06	20.95	+62:45	PO	19.63	19.53	+63:09	YR	20.89	20.78	+59:48	PO	19.08	18.98
	5	+62:04	YR	21.35	21.24	+64:09	PO	19.99	19.88	+63:37	YR	21.97	20.86	+60:20	PO	19.08	18.98
	6	+62:35	μCT scanned			+64:39	μCT scanned			+64:19	μCT scanned			+60:55	μCT scanned		
t90	1	+91:43	YR	21.57	21.46	+87:40	PO	18.81	18.71	+90:55	YR	19.45	19.35	+87:36	PO	18.13	18.03
	2	+92:20	YR	22.32	22.20	+88:12	PO	19.83	19.72	+91:32	YR	21.23	21.12	+88:25	PO	18.38	18.28
	3	+92:51	YR	20.78	20.67	+88:44	PO	19.49	19.38	+92:04	YR	19.36	19.26	+88:56	PO	17.76	17.66
	4	+93:23	YR	21.31	21.20	+89:16	PO	19.73	19.63	+92:37	YR	19.45	19.35	+89:32	PO	18.19	18.10
	5	+93:54	YR	21.58	21.47	+89:47	PO	19.50	19.40	+93:08	YR	19.45	19.35	+90:03	PO	17.82	17.73
t120	1	+121:17	YR	22.28	22.16	+119:39	PO	18.89	18.79	+121:42	YR	20.68	20.57	+116:46	PO	18.23	18.14
	2	+121:49	YR	21.46	21.34	+120:15	PO	18.87	18.77	+122:18	YR	19.72	19.62	+117:24	PO	20.04	19.93
	3	+122:18	YR	21.16	21.05	+120:51	YR	19.72	19.61	+122:51	YR	20.68	20.57	+117:59	PO	18.93	18.83
	4	+122:49	YR	20.65	20.55	+122:23	PO	19.72	19.61	+123:24	YR	20.68	20.57	+118:32	PO	20.47	20.37
	5	+123:19	YR	20.53	20.42	+122:57	PO	18.94	18.84	+123:58	YR	21.00	20.89	+119:06	PO	20.23	20.12
	6	+123:51	μCT scanned			+123:31	μCT scanned			+124:32	μCT scanned			+119:37	μCT scanned		
t160	1	+161:45	YR	22.14	22.02	+157:11	YR	20.77	20.66	+160:06	YR	20.33	20.23	+157:54	PO	19.89	19.79
	2	+162:17	YR	21.11	21.00	+157:55	YR	19.71	19.61	+160:38	YR	20.59	20.49	+158:24	YR	20.68	20.57
	3	+162:49	YR	21.03	20.92	+158:27	PO	20.51	20.40	+161:13	YR	20.22	20.11	+158:56	PO	20.26	20.16
	4	+163:21	YR	21.03	20.92	+158:57	YR	20.88	20.76	+161:45	YR	20.33	20.23	+159:26	YR	20.83	20.72
	5	+164:03	YR	21.46	21.35	+159:27	YR	20.23	20.12	+162:16	YR	20.33	20.23	+159:58	YR	20.77	20.66
t200	1	+201:09	YR	21.36	21.24	+198:04	PO	20.32	20.22	+200:32	YR	19.47	19.37	+196:55	YR	20.92	20.81
	2	+201:49	YR	21.16	21.04	+198:41	PO	20.77	20.66	+201:03	YR	20.92	20.81	+197:26	YR	20.87	20.76
	3	+202:19	YR	20.79	20.68	+199:17	YR	20.76	20.65	+201:36	YR	20.53	20.42	+197:56	YR	20.27	20.16
	4	+202:45	YR	21.39	21.28	+199:49	PO	20.92	20.81	+202:05	YR	19.47	19.37	+198:28	PO	21.10	20.99
	5	+203:18	YR	20.61	20.50	+200:19	YR	20.20	20.10	+202:42	YR	19.47	19.37	+198:59	YR	20.73	20.62
	6	+203:50	μCT scanned			+200:47	μCT scanned			+203:16	μCT scanned			+199:29	μCT scanned		
Cast	1	Preplaced	PO	20.54	20.43	Preplaced	PO	14.27	14.20	Preplaced	YR	21.40	21.29	Preplaced	PO	14.24	14.17
	2	Preplaced	PO	20.23	20.12	Preplaced	PO	18.51	18.41	Preplaced	PO	20.39	20.28	Preplaced	PO	14.24	14.17
	3	Preplaced	YR	19.06	18.96	Preplaced	PO	13.99	13.92	Preplaced	PO	20.89	20.78	Preplaced	PO	20.25	20.14
	4	Preplaced	PO	19.52	19.42	Preplaced	PO	19.34	19.23	Preplaced	YR	21.13	21.02	Preplaced	PO	17.97	17.88
	5	Preplaced	PO	19.98	19.87	Preplaced	PO	12.53	12.46	Preplaced	YR	19.31	19.21	Preplaced	PO	16.07	15.98
	6	Preplaced	μCT scanned			Preplaced	μCT scanned			Preplaced	μCT scanned			Preplaced	μCT scanned		

PO - Pull-out of reinforcement; YR - Yielding of reinforcement

References

[1] F. Craveiro, J.P. Duarte, H. Bartolo, P.J. Bartolo, Additive manufacturing as an enabling technology for digital construction: A perspective on construction 4.0, Autom. Constr. 103 (2019) 251–267, https://doi.org/10.1016/j.autcon.2019.03.011.

[2] Buswell R.A. et al. (2022) Digital fabrication with cement-based materials: process classification and case studies. In: Roussel N., Lowke D. (eds) Digital Fabrication with Cement-Based Materials. RILEM State-of-the-Art Reports, vol 36. Springer, Cham. https://doi.org/10.1007/978-3-030-90535-4_2.

[3] R.A. Buswell, W.R.L. da Silva, F.P. Bos, H.R. Schipper, D. Lowke, N. Hack, H. Kloft, V. Mechtcherine, T. Wangler, N. Roussel, A process classification framework for defining and describing digital fabrication with concrete, Cem. Concr. Res. 134 (2020), 106068, https://doi.org/10.1016/j.cemconres.2020.106068.

[4] T. Wangler, N. Roussel, F.P. Bos, T.A.M. Salet, R.J. Flatt, Digital concrete: a review, Cem. Concr. Res. 123 (2019), 105780, https://doi.org/10.1016/j.cemconres.2019.105780.

[5] F.P. Bos, C. Menna, M. Pradena, et al., The realities of additively manufactured concrete structures in practice, Cem. Concr. Res. 156 (2022), 106746.

[6] B. Khoshnevis, Automated construction by contour crafting—related robotics and information technologies, Autom. ConStruct. 13 (2004) 5–19, https://doi.org/10.1016/j.autcon.2003.08.012.

[7] D. Asprone, C. Menna, F.P. Bos, T.A.M. Salet, J. Mata-Falcón, W. Kaufmann, Rethinking reinforcement for digital fabrication with concrete, Cem. Concr. Res. 112 (2018) 111–121, https://doi.org/10.1016/j.cemconres.2018.05.020.

[8] T. Marchment, J. Sanjayan, Bond properties of reinforcing bar penetrations in 3D concrete printing, Autom. Constr. 120 (2020), 103394.

[9] N. Freund, I. Dressler, D. Lowke, Studying the Bond Properties of Vertical Integrated Short Reinforcement in the Shotcrete 3D Printing Process. In: Bos, F., Lucas, S., Wolfs, R., Salet, T. (eds) Second RILEM International Conference on Concrete and Digital Fabrication. DC 2020. RILEM Bookseries, vol 28. Springer, Cham. https://doi.org/10.1007/978-3-030-49916-7_62.

[10] L. Hass, F. Bos, Bending and pull-out tests on a novel screw type reinforcement for extrusion-based 3D printed concrete, in: F.P. Bos, S.S. Lucas, R.J.M. Wolfs, T.A.M. Salet (Eds.), Second RILEM International Conference on Concrete and Digital Fabrication, Springer International Publishing, Cham, 2020, pp. 632–645.

[11] Winsun. Demonstrating the viability of 3D printing at construction scale, future of construction, 2016. doi:http://www.winsun3d.com/En/.

[12] G.P.J.A. Goris, Traditional reinforcement in 3D concrete printed structures, 2018. doi: https://research.tue.nl/en/studentTheses/traditional-reinforcement-in-3d-concrete-printed-structures.

[13] G. Grasser, L. Pammer, H. Köll, E. Werner, F.P. Bos, Complex architecture in printed concrete: The case of the innsbruck university 350th anniversary pavilion COHESION, in: F.P. Bos, S.S. Lucas, R.J.M. Wolfs, T.A.M. Salet (Eds.), Second RILEM International Conference on Concrete and Digital Fabrication, Springer International Publishing, Cham, 2020, pp. 1116–1127.

[14] D. Asprone, F. Auricchio, C. Menna, V. Mercuri, 3D printing of reinforced concrete elements: Technology and design approach, Constr. Build. Mater. 165 (2018) 218–231, https://doi.org/10.1016/j.conbuildmat.2018.01.018.

[15] T.A.M. Salet, Z.Y. Ahmed, F.P. Bos, H.L.M. Laagland, Design of a 3D printed concrete bridge by testing, Virtual Phys. Prototyp. 13 (2018) 222–236, https://doi.org/10.1080/17452759.2018.1476064.

[16] F.P. Bos, Z.Y. Ahmed, E.R. Jutinov, T.A.M. Salet, Experimental exploration of metal cable as reinforcement in 3D printed concrete, Materials 10 (2017), https://doi.org/10.3390/ma10111314.

[17] L. Demont, N. Ducoulombier, R. Mesnil, J.-F. Caron. Flow-Based Pultrusion of continuous fibers for cement-based composite material and additive manufacturing: rheological and technological requirements. Composite Structures, 262(August 2020) (2021), 113564. https://doi.org/10.1016/j.compstruct.2021.113564.

[18] V. Mechtcherine, A. Michel, M. Liebscher, T. Schmeier, Extrusion-based additive manufacturing with carbon reinforced concrete: concept and feasibility study, Materials 13 (2020), https://doi.org/10.3390/ma13112568.

[19] T. Marchment, J. Sanjayan, Mesh reinforcing method for 3D concrete printing, Autom. Constr. 109 (2020), 102992, https://doi.org/10.1016/j.autcon.2019.102992.

[20] A. Perrot, Y. Jacquet, D. Rangeard, E. Courteille, M. Sonebi, Nailing of layers: a promising way to reinforce concrete 3D printing structures, Materials 13 (2020), https://doi.org/10.3390/ma13071518.

[21] O. Geneidy, S. Kumarji, A. Dubor, A. Sollazzo, Simultaneous reinforcement of concrete while 3D printing, in: F.P. Bos, S.S. Lucas, R.J.M. Wolfs, T.A.M. Salet (Eds.), Second RILEM International Conference on Concrete and Digital Fabrication, Springer International Publishing, Cham, 2020, pp. 895–905.

[22] V.C. Li, F.P. Bos, K. Yu, W. McGee, T.Y. Ng, S.C. Figueiredo, K. Nefs, V. Mechtcherine, V.N. Nerella, J. Pan, G.P.A.G. van Zijl, P.J. Kruger, On theemergence of 3D printable engineered, strain hardening cementitious composites (ECC/SHCC), Cement Concr. Res. 132 (2020), 106038, https://doi.org/10.1016/j. cemconres.2020.106038.

[23] M. Hambach, D. Volkmer, Properties of 3D-printed fiber-reinforced Portlandcement paste, Cement Concr. Compos. 79 (2017) 62–70, https://doi.org/10.1016/j.cemconcomp.2017.02.001.

[24] F.P. Bos, E. Bosco, T.A.M. Salet, Ductility of 3D printed concrete reinforced with short straight steel fibers, Virtual Phys. Prototyp. 14 (2019) 160–174, https://doi.org/10.1080/17452759.2018.1548069.

[25] A.R. Arunothayan, B. Nematollahi, R. Ranade, S.H. Bong, J. Sanjayan, Development of 3D-printable ultra-high performance fiber-reinforced concrete fordigital construction, Constr. Build. Mater. 257 (2020), 119546, https://doi.org/10.1016/j.conbuildmat.2020.119546.

[26] H. Ogura, V. Nerella, V. Mechtcherine, Developing and testing of strain-hardening cement-based composites (SHCC) in the context of 3D-printing, Materials 11 (2018) 1375, https://doi.org/10.3390/ma11081375.

[27] B. Zhu, J. Pan, B. Nematollahi, Z. Zhou, Y. Zhang, J. Sanjayan, Development of 3D printable engineered cementitious composites with ultra-high tensile ductility fordigital construction, Mater. Des. 181 (2019), 108088, https://doi.org/10.1016/j. matdes.2019.108088.

[28] S. Chaves Figueiredo, C. Romero Rodríguez, Z.Y. Ahmed, D.H. Bos, Y. Xu, T. M. Salet, O. Çopuroˇglu, E. Schlangen, F.P. Bos, Mechanical behavior of printedstrain hardening cementitious composites, Materials 13 (2020) 2253, https://doi. org/10.3390/ma13102253.

[29] RC 6 Bond test for reinforcement steel. 2. Pull-out test, 1983, doi: 10.1617/2351580117.081.

[30] ACI Committee 408, ACI 408R-03: Bond and Development of Straight Reinforcing Bars in Tension. http://civilwares.free.fr/ACI/MCP04/408r_03.PDF.

[31] F. Bos, R. Wolfs, Z. Ahmed, T. Salet, Additive manufacturing of concrete in construction: Potentials and challenges of 3D concrete printing, Virtual Phys. Prototyp 11 (2016) 209–225, https://doi.org/10.1080/17452759.2016.1209867.

[32] V. Mechtcherine, F.P. Bos, A. Perrot, W.R.L. da Silva, V.N. Nerella, S. Fataei, R.J. M. Wolfs, M. Sonebi, N. Roussel, Extrusion-based additive manufacturing with cement-based materials – production steps, processes, and their underlying physics: A review, Cem. Concr. Res. 132 (2020), 106037, https://doi.org/10.1016/j.cemconres.2020.106037.

[33] Data sheet for Weber 145-2. https://www.3d.weber/materials/.

[34] Data sheet for italcementi i.tech 3D N. https://www.italcementi.it/it/system/files_force/assets/document/fd/fe/tech_data_sheet_i.tech_3d_n_en.pdf?download=1.

[35] E.T. Assessment, n.d. European technical assessment ETA-12/0114 of 12/10/2017. doi:https://downloads.spax.com.

[36] 3D Concrete Printing Research Group at Eindhoven University of Technology (2021). Salad Slicer v0.2.0: A slicer for 3D concrete printing. URL: https://github.com/3DCP-TUe/SaladSlicer.

[37] Arjen Deetman, Gabriel Rumpf, Benedikt Wannemacher, Mohamed Dawod, Zuardin Akbar, Andrea Rossi (2021). Robot Components v1.1.0: Intuitive Robot Programming for ABB Robots inside of Rhinoceros Grasshopper. URL https://github.com/RobotComponents/RobotComponents https://doi.org/10.5281/zenodo.5773815.

[38] F.P. Bos, S. Dezaire, Z.Y. Ahmed, A. Hoekstra, T.A.M. Salet. Bond of Reinforcement Cable in 3D Printed Concrete. In F. Bos, S. Lucas, R. Wolfs, & T. Salet (Eds.), Second RILEM International Conference on Concrete and Digital Fabrication: Digital Concrete 2020 (2020) (pp. 584-600). (RILEM Bookseries; Vol. 28). Springer. https://doi.org/10.1007/978-3-030-49916-7_60.

[39] L. Hass, F.P. Bos. Robotically placed reinforcement using the Automated Screwing Device – an application perspective for 3D concrete printing. in: Digit. Concr. 2022, 3rd RILEM Int. Conf. Concr. Digit. Fabr., 2022: p. Submitted.

[40] Image reconstruction software: VGStudio. https://www.volumegraphics.com/en/products/vgstudio.html.

[41] Image post processing software: ImageJ. https://imagej.net/.

[42] N. Phansalkar, S. More, A. Sabale, M. Joshi, Adaptive local thresholding for detection of nuclei in diversity stained cytology images, in: *2011 International Conference on Communications and Signal ProcessIng.* IEEE, 2011, https://doi.org/10.1109/iccsp.2011.5739305.

[43] F.P. Bos, J. Kruger, S.S. Lucas, G. van Zijl, Juxtaposing fresh material characterisation methods for buildability assessment of 3D printable cementitious mortars, Cement Concr. Compos. 120 (2021) [104024], https://doi.org/10.1016/j.cemconcomp.2021.104024.

[44] R.J.M. Wolfs, F.P. Bos, T.A.M. Salet, Correlation between destructive compression tests and non-destructive ultrasonic measurements on early age 3D printed concrete, Constr. Build. Mater. 181 (2018) 447–454, https://doi.org/10.1016/j.conbuildmat.2018.06.060.

[45] Z.Y. Ahmed, R.J.M. Wolfs, F.P. Bos, T.A.M. Salet, A framework for large-scale structural applications of 3D printed concrete: the case of a 29 m Bridge in the Netherlands, Open Conf. Proc. 1 (2022) 5–19, https://doi.org/10.52825/ocp.v1i.74.

[46] R.J.M. Wolfs, F.P. Bos, T.A.M. Salet, Early age mechanical behaviour of 3D printed concrete: Numerical modelling and experimental testing, Cem. Concr. Res. 106 (2018) 103–116, https://doi.org/10.1016/j.cemconres.2018.02.001.

[47] B. Baz, G. Aouad, P. Leblond, O. Al-Mansouri, M. D'hondt, S. Remond, Mechanical assessment of concrete - steel bonding in 3D printed elements, Constr. Build. Mater. 256 (2020) 119457, https://doi.org/10.1016/j.conbuildmat.2020.119457.

[48] European Committee. EN 1992-1-1 Eurocode 2: Design of Concrete Structures—Part 1-1: General Ruels and Rules for Buildings. *European Committee: Brussels, Belgium* (2005).

[49] F.P. Bos, L. Hass. Assembly for guiding a helical body into a viscous, pliable, or solidifying material. Manuscript submitted for publication (2021). (Patent No. N2030291).

[50] V. Mechtcherine, R. Buswell, H. Kloft, F.P. Bos, N. Hack, R. Wolfs, J. Sanjayan, B. Nematollahi, E. Ivaniuk, T. Neef, Integrating reinforcement in digital fabrication with concrete: A review and classification framework, Cement Concr. Compos. 119 (2021), 103964.

[51] V. Mechtcherine, K. van Tittelboom, A. Kazemian, et al., A roadmap for quality control of hardening and hardened printed concrete, Cem. Concr. Res. 157 (2022), 106800.

[52] NEN-EN 196-1, Methods of Testing Cement — Part 1: Determination of Strength.

[53] EN 196-3 Methods of testing cement — Part 3: Determination of setting times and soundness.

[54] EN 1015-9 Methods of test for mortar for masonry - Part 9: Determination of workable life and correction time of fresh mortar.